On the use of phase correction rings on Fresnel zone plates with ultrasound piston emitters

Sergio Pérez-López,[1] José Miguel Fuster,[2,a)] Pilar Candelas,[1,3] Constanza Rubio,[1,3] and Francisco Belmar[1,3]

[1]*Centro de Tecnologías Físicas, Universitat Politècnica de València, 46022 Valencia, Spain*
[2]*D. Comunicaciones, Universitat Politècnica de València, 46022 Valencia, Spain*
[3]*D. Física Aplicada, Universitat Politècnica de València, 46022 Valencia, Spain*

In this work, the distortion of the Fresnel Zone Plate focusing profile generated by a piston emitter in ultrasound applications is significantly reduced through the use of phase correction rings, which compensate the effect of the piston emitter radiation diagram. Both simulation and experimental results demonstrate the improvement achieved with this design method over the conventional case.

Wave focusing is a hot topic of great interest in many areas of physics, including optics, x-rays, microwaves, or ultrasounds.[1–4] Fresnel Zone Plates (FZPs) have been proposed for implementing this application in situations where conventional lenses are difficult to implement or planar fabrication is advantageous.[5]

Conventional FZPs are capable of focusing a planar wave into a certain location with a single focus. The structure of the FZP is a set of concentric rings with increasing radius, each ring being a Fresnel region. The radius and width of each Fresnel ring depends on certain design parameters such as the desired focal length and the signal wavelength.

The use of FZPs in the ultrasound domain is very appealing because it provides high flexibility in certain medical applications where fast and accurate focus shifting is critical,[6] such as tumor ablation.[7–9] Other approaches have also been proposed, such as lenses based on passive acoustic metamaterials[10] and multi-array devices.[11,12] Metamaterials provide several interesting applications, such as acoustic cloaking, although they are complex structures difficult to build. Multi-array devices are expensive systems that require Magnetic Resonance Imaging (MRI) real-time monitoring to adjust the amplitudes and phases of the emitting elements in order to focus at the intended treatment area. Therefore, FZPs are still a more attractive alternative for conventional focusing applications as they are cheaper and simpler to use.

Planar and spherical wave incidence have been extensively studied,[4] and FZPs can be easily designed for such excitations. However, ultrasonic FZPs usually require the use of piston emitters,[13–15] which in certain situations introduce a significant distortion on the focus profile. This work demonstrates that an accurate focus profile is achieved when the piston emitter parameters are included in the design process of ultrasonic FZPs.

The governing equation used to design a FZP with point source excitation is given by

$$d + F + n\frac{\lambda}{2} = \sqrt{d^2 + r_n^2} + \sqrt{F^2 + r_n^2}, \qquad (1)$$

with $n = 1, 2, ..., N$, being N the number of Fresnel regions, F the FZP focal length, λ the operating wavelength, d the separation between the point source and the FZP, and r_n the radius of each Fresnel region. Using Eq. (1), the r_n values are obtained from the FZP design parameters (F, N, λ, and d).

Figure 1 shows a setup with a FZP placed at a distance d of a piston emitter in the ultrasound domain. In the far field case, the piston can be modeled as a point source emitter with a specific directivity pattern, given by

$$D = \frac{2J_1(ka\sin(\theta))}{ka\sin(\theta)}, \qquad (2)$$

with k being the wave number, a the piston active radius, θ the angle referenced to the normal direction of the piston surface, and J_1 the first kind and first order Bessel function.

Figure 2 shows the directivity of a piston with a combined ka product of 16.96. As it can be observed, the piston introduces two drawbacks over the ideal point source emitter: the non-omnidirectional behavior and the π-phase change at some secondary lobes. This second drawback is more significant, because the additional π-phase introduced in the secondary lobes causes that their contributions destructively interfere those of the main lobe, which results in a significant distortion at the focusing profile. Thus, the maximum angle θ_{max} beyond which there would be a phase error due to the piston directivity diagram can be calculated
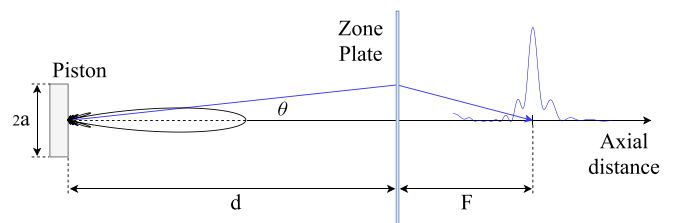

FIG. 1. Ultrasound FZP focusing setup using a piston emitter.

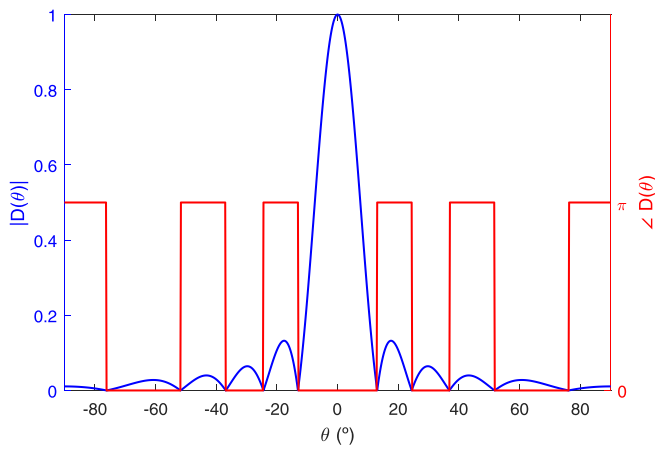a)Electronic mail: jfuster@dcom.upv.es

FIG. 2. Directivity pattern of a piston emitter with $ka = 16.96$; module (blue) and phase (red).

from the first zero of the $J_1(x)$ function, which is located at $x = 3.83$, using

$$\theta_{max} = \arcsin\left(\frac{3.83}{ka}\right). \tag{3}$$

From the θ_{max} parameter obtained with Eq. (3), it is possible to calculate the FZP maximum radius as

$$R_{max} = d \tan(\theta_{max}). \tag{4}$$

Equations (1) and (4) yield to a maximum number of radii for the FZP in order to avoid phase distortion

$$N_{max} = \left\lfloor \frac{2}{\lambda}\left(\sqrt{d^2 + R_{max}^2} + \sqrt{F^2 + R_{max}^2} - d - F\right)\right\rfloor, \tag{5}$$

with $\lfloor \cdot \rfloor$ being the floor operator.

If $N > N_{max}$, the π-phase error introduced by the piston first secondary lobes results in a destructive interference at the focal length, as mentioned earlier. Figure 3 shows the computed axial intensity of the same FZP with $N = 31$ for both an ideal point source emitter (blue line) and a piston

emitter with $ka = 16.96$, $d = 340$ mm and $N_{max} = 14$ (red line). The FZP has been designed to operate at $\lambda = 5.55$ mm with $F = 80$ mm. As it can be observed from the figure, the phase error generates a very noticeable distortion on the focusing profile, which can result in malfunctioning of the FZP. It is worth noting that at the focal length, the acoustic intensity shifts from a maximum value in the point emitter case to a local minimum in the piston case.

The interference behavior of each Fresnel region can be analyzed by plotting the directivity phase and the FZP radii in the same graph, as shown in Fig. 4. Thus, those Fresnel regions in which the piston phase is π generate a destructive interference, whereas those radii in which the piston phase is 0 generate a constructive interference.

In order to correct the phase error, a phase correction ring (PCR) must be added to the FZP when $N > N_{max}$ so the π-phase change is compensated. The PCR consists of skipping one Fresnel radius when the $n > N_{max}$ condition is reached in Eq. (1); therefore, introducing an additional phase shift of π that compensates the piston phase error. This PCR should be added every time the FZP radius changes from a piston directivity lobe to the next one.

Figure 5 shows two different FZPs using piston emitters with the same number of Fresnel regions ($N = 31$) and their corresponding focusing profiles. Figures 5(a) and 5(c) correspond to a conventional FZP, while Figs. 5(b) and 5(d) are associated with the FZP with one PCR. In both simulations, $ka = 16.96$, and the distance between the piston and the FZP is 340 mm. As it can be observed from the comparison of Figs. 5(c) and 5(d), the PCR removes the phase error introduced by the piston and achieves a focal length of 80 mm, which corresponds to the theoretically designed focal length. However, there is still some remnant distortion introduced by the piston due to the amplitude of its directivity pattern, which cannot be compensated and increases the level of the side lobes adjacent to the main focus.

Figure 6 shows additional simulation results for two different focal lengths: $F = 60$ mm [Fig. 6(a)] and $F = 100$ mm [Fig. 6(b)]. Blue lines correspond to conventional FZP
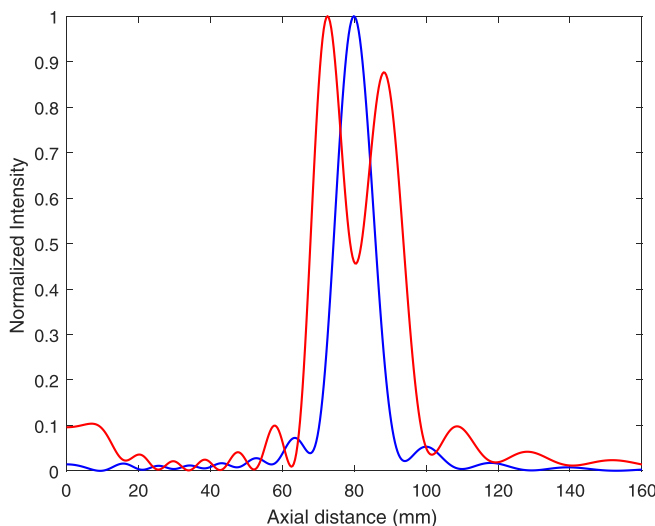

FIG. 3. Normalized axial intensity of a FZP with $N = 31$, $F = 80$ mm, and $\lambda = 5.55$ mm. Ideal point source emitter (blue line) and piston emitter with $ka = 16.96$ and $d = 340$ mm (red line).
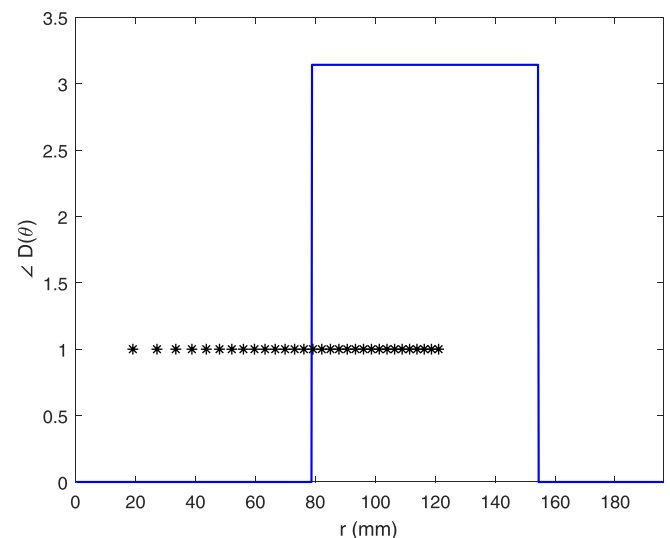

FIG. 4. FZP radii (black) and directivity phase for a piston with $ka = 16.96$ and $d = 340$ mm (blue), $N = 31$, $F = 80$ mm, and $\lambda = 5.55$ mm.
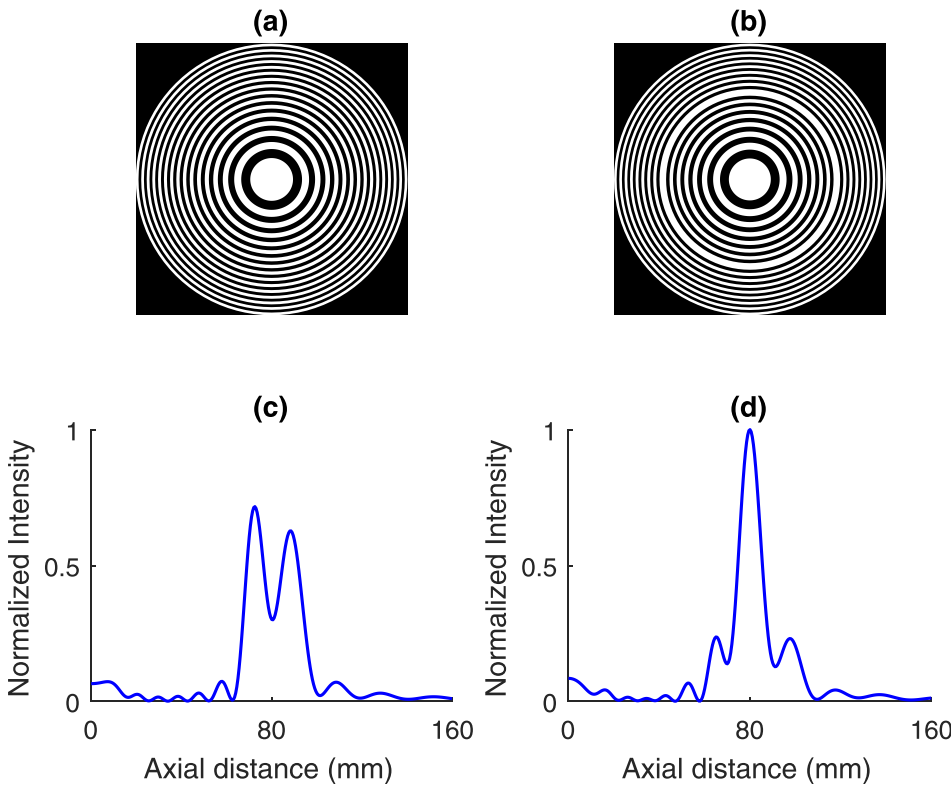
(a)

(b)

(c)

(d)

FIG. 5. (a) Conventional FZP layout and (c) its normalized axial intensity. (b) FZP with PCR and (d) its normalized axial intensity; $N = 31$, $F = 80$ mm, $\lambda = 5.55$ mm, $ka = 16.96$, and $d = 340$ mm.

focusing profiles, while red lines are used to plot focusing profiles for the FZP with one PCR. Comparing the focusing profiles plotted in Figs. 5 and 6, it can be deduced that the distortion augments with the focal length. This is caused by the increase in the FZP size, as the radii of the different Fresnel regions become higher with the focal length, which results in a bigger θ parameter in the piston directivity pattern, introducing more amplitude and phase distortion onto the FZP focusing profile. In the conventional FZP case, the increase in distortion can be observed in the destructive interference at the focus, which becomes more significant when F is higher. In the FZP-PCR case, the overall distortion is much lower, because phase distortion has been removed

with the PCR. However, the remnant amplitude distortion is still present, and it also augments with focal length, as it can be deduced by observing the increasing level of the side lobes adjacent to the main focus.

In order to evaluate the distortion introduced by the piston, Fig. 7 shows the computed acoustic intensity at the focal length as a function of N for three different FZPs: a conventional FZP (red line), a FZP with one PCR (blue line) and a FZP with two PCRs (black line). The boundary between the main lobe and the first secondary lobe is located at $N_{max1} = 14$ and the boundary between the first secondary lobe and the next one is located at $N_{max2} = 45$. As it can be observed from Fig. 7, when $N > 14$, the focal intensity of the conventional
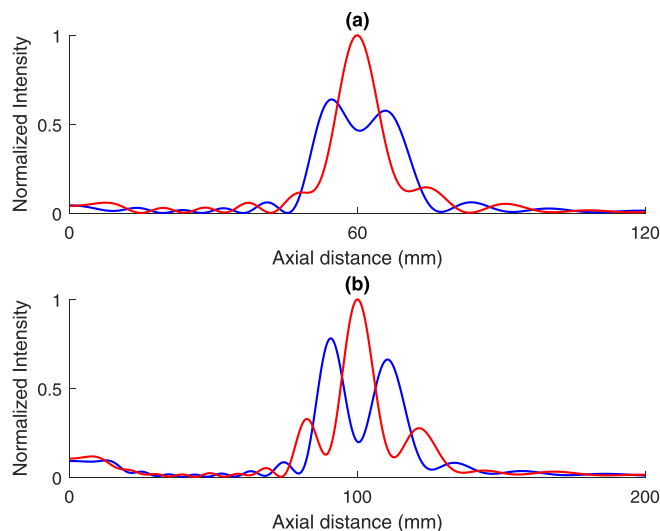

FIG. 6. Axial intensity profiles for conventional FZP (blue line) and FZP with PCR (red line): (a) $F = 60$ mm, (b) $F = 100$ mm; $N = 31$, $\lambda = 5.55$ mm, $ka = 16.96$, and $d = 340$ mm.
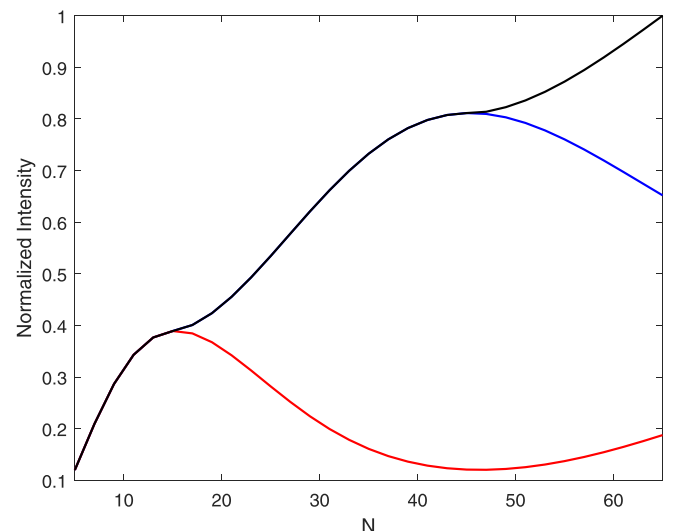

FIG. 7. Normalized intensity at focal length: Conventional FZP (red), FZP with one PCR (blue) and FZP with two PCRs (black). $ka = 16.96$, $d = 340$ mm, $N_{max1} = 14$, and $N_{max2} = 45$.
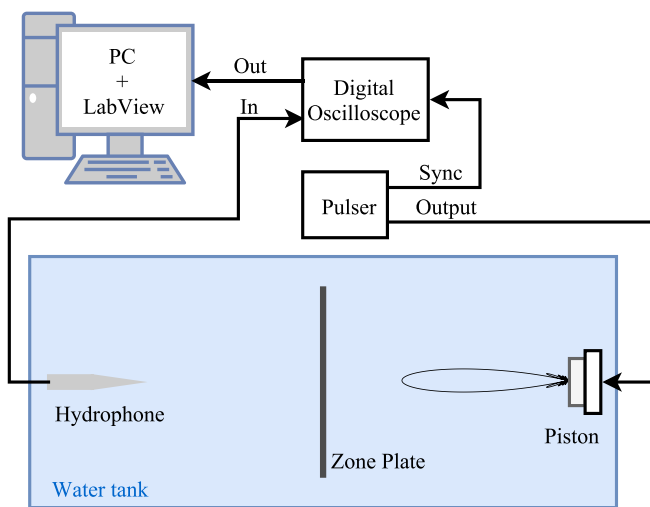
FIG. 8. Experimental set-up.

FZP does not increase when N increases as expected, but instead it begins to decrease due to the destructive interferences generated by the $N_{max1} < N < N_{max2}$ Fresnel regions. The FZP with one PCR compensates the phase error up to $N = N_{max2}$. As this FZP does not have the second PCR, when $N > 45$, the intensity at the focal length begins to decrease, while it starts to increase again for the conventional case. This phenomenon is due to the fact that for $N > 45$ the phase of the piston directivity pattern is not π but 0 again, due to the change to the next secondary lobe. Finally, the last FZP includes two PCRs for compensating the phase error due to both transitions in the piston phase diagram and presents a proper behavior. In this last case, the intensity at the focus is continuously increasing because all the contributions are constructive. This mechanism can be extended, adding additional PCRs when the number of Fresnel regions increases and more piston side lobes contribute to the FZP focusing profile.

The simulation results have been validated through experimental measurements. Figure 8 shows the experimental set-up. An underwater 3D automated positioning system with a spatial resolution of $1 \times 1 \times 1 \, mm^3$ is used inside a water tank. An Imasonic piston transducer with a 30 mm active diameter, a central frequency of 260.88 kHz and a -6 dB bandwidth of 180.66 kHz is used as an emitter. A needle hydrophone from Precision Acoustics, Ltd., with a diameter of 1.5 mm and a -4 dB bandwidth that goes from 200 kHz to 25 MHz is used as receiver. The transmitted
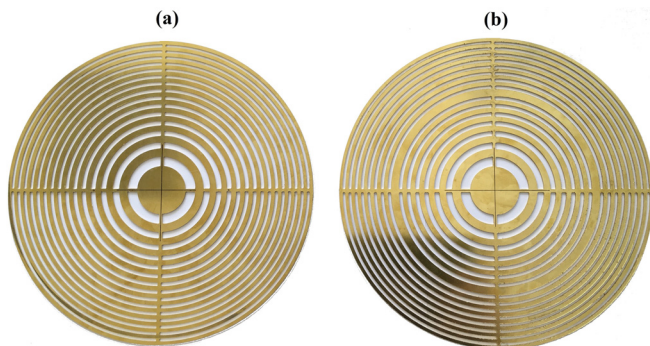

FIG. 9. (a) Conventional FZP with $R_L = 122.11$ mm (b) FZP-PCR with $R_L = 123.51$ mm.
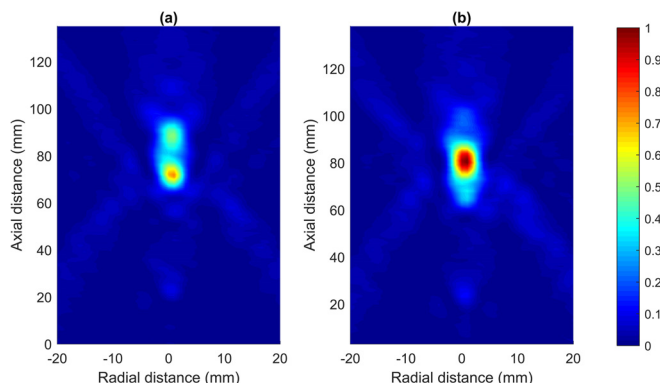

FIG. 10. Experimental acoustic intensity maps: conventional FZP (a) and FZP with PCR (b).

signal is generated using a Panametrics 5077PR Pulser, whereas the received signal is acquired and sampled using a digital oscilloscope from Pico Technology with 12-bit resolution and 72 dB dynamic range.

Two Soret FZPs have been measured in the experiment, a conventional FZP [Fig. 9(a)] and the FZP with a PCR [Fig. 9(b)]. The FZP external radii are $R_L = 122.11$ mm and $R_L = 123.51$ mm, respectively. Both lenses are very similar in size as they differ in a single Fresnel region. The FZPs are 1 mm thick and made of brass. They have been designed for operating at 270 kHz at a focal length of 80 mm. The number of Fresnel zones is 31, and the separation between the piston and the zone plate is 340 mm. The water sound speed is $c_w = 1500$ m/s.

Figure 10 shows the acoustic intensity maps for both the conventional FZP [Fig. 10(a)] and the FZP with one PCR [Fig. 10(b)]. Both maps have been normalized to the same reference, the maximum value in the FZP-PCR case. As it can be observed from the figure, the focal length of the FZP with one PCR agrees accurately with the design value of 80 mm, while the focusing profile of the conventional FZP is severely distorted, and its main focus is shift to 10 mm towards the lens plane.
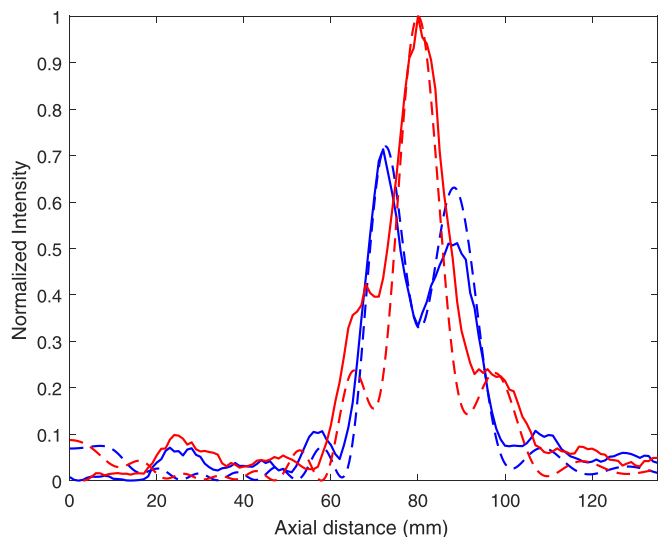

FIG. 11. Axial focusing profiles for conventional FZP: measurements (blue solid line) and simulation (blue dashed line) and FZP with PCR: measurements (red solid line) and simulation (red dashed line).
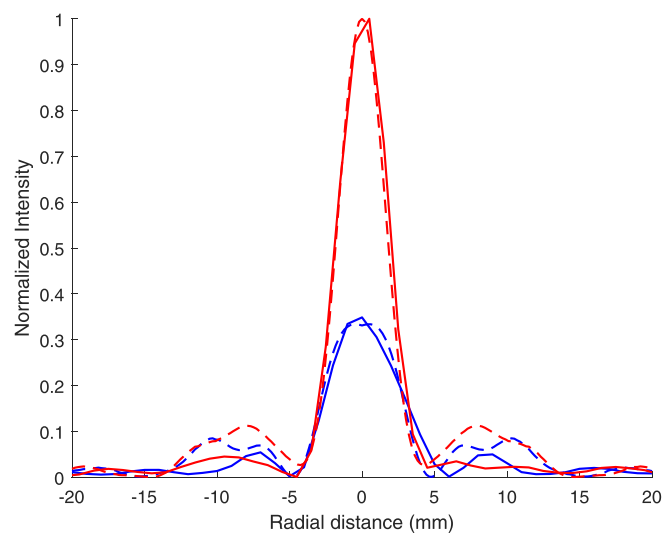
FIG. 12. Radial focusing profiles for conventional FZP: measurements (blue solid line) and simulation (blue dashed line) and FZP with PCR: measurements (red solid line) and simulation (red dashed line).

Figure 11 shows the measured focusing profiles along the axial direction for both lenses: conventional FZP (blue) and FZP with one PCR (red). The corresponding simulation results are also depicted as dashed lines. As it can be observed from Fig. 11, experimental results agree very well with simulations, and the FZP with the correction ring achieves its theoretical focal length of 80 mm, whereas the standard FZP presents destructive interference at that same focal length.

Figure 12 shows the measured focusing profiles along the radial direction for both lenses: conventional FZP (blue) and FZP with one PCR (red). The corresponding simulation results are also depicted as dashed lines. As it can be observed from Fig. 12, experimental results also agree very well with simulations, and the FZP with one PCR presents a narrower beam waist ($\omega_0 = 5.98$ mm) than the conventional FZP ($\omega_0 = 7.66$ mm). Both values are higher than the theoretical minimum value,[16] which in this case corresponds to $\omega_0 = 2.31$ mm.

Although experimental and simulation results agree very well in Figs. 11 and 12, there are small differences that can be caused by the cross-shaped mechanical support that can be observed in Fig. 9, which maintains the FZP brass rings fixed in place. This cross-shaped structure has not been modelled in the simulation.

In this paper, a method to design FZPs to operate with piston emitters, which are typically used for underwater ultrasound transmission, has been presented. A theoretical analysis on the error introduced by the piston has been developed, and a method to eliminate the piston phase error based on PCRs has been proposed. Simulation results have been obtained to validate the theoretical model. Moreover, the performance of these FZPs with PCRs has been experimentally demonstrated showing an improvement over conventional FZPs and removing the focusing profile distortion caused by the phase error introduce by piston emitters.

[1]S. Tamura, M. Yasumoto, N. Kamijo, A. Takeuchi, K. Uesugi, Y. Terada, and Y. Suzuki, Vacuum **84**, 578 (2009).
[2]H. D. Hristov and J. M. Rodriguez, IEEE Microwave Wireless Compon. Lett. **22**, 574 (2012).
[3]R. Yang, W. Tang, and Y. Hao, Opt. Express **19**, 12348 (2011).
[4]D. C. Calvo, A. L. Thangawng, M. Nicholas, and C. N. Layman, Appl. Phys. Lett. **107**, 014103 (2015).
[5]S. M. Stout-Grandy, A. Petosa, I. V. Minin, O. V. Minin, and J. Wight, IEEE Trans. Antennas Propag. **54**, 3629 (2006).
[6]J. Fuster, P. Candelas, S. Castiñeira-Ibáñez, S. Pérez-López, and C. Rubio, Sensors **17**, 2809 (2017).
[7]J. Kennedy, F. Wu, G. ter Haar, F. Gleeson, R. Phillips, M. Middleton, and D. Cranston, Ultrasonics **42**, 931 (2004).
[8]D. Suo, Z. Jin, X. Jiang, P. A. Dayton, and Y. Jing, Appl. Phys. Lett. **110**, 023703 (2017).
[9]D. Suo, S. Guo, W. Lin, X. Jiang, and Y. Jing, Phys. Med. Biol. **60**, 7403 (2015).
[10]C. Shen, J. Xu, N. X. Fang, and Y. Jing, Phys. Rev. X **4**, 041033 (2014).
[11]A. Carovac, F. Smajlovic, and D. Junuzovic, Acta Inf. Med. **19**, 168 (2011).
[12]Y. Xie, C. Shen, W. Wang, J. Li, D. Suo, B.-I. Popa, Y. Jing, and S. A. Cummer, Sci. Rep. **6**, 35437 (2016).
[13]H. Estrada, A. Uris, and F. Meseguer, Appl. Phys. Lett. **101**, 104103 (2012).
[14]M. Martins, V. Correia, J. Cabral, S. Lanceros-Mendez, and J. Rocha, Sens. Actuators A: Phys. **184**, 141 (2012).
[15]T.-D. Luong, T. Hies, and C.-D. Ohl, Sci. Rep. **6**, 36096 (2016).
[16]D. R. Smith, V. R. Gowda, O. Yurduseven, S. Larouche, G. Lipworth, Y. Urzhumov, and M. S. Reynolds, J. Appl. Phys. **121**, 014901 (2017).